Synthesis and characterization of silica sand-derived nano-forsterite ceramics

Upik Nurbaiti[a,b], Darminto[a], Triwikantoro[a], Mochamad Zainuri[a], Suminar Pratapa[a,*]

[a] Department of Physics, Faculty of Mathematics and Sciences, Institute of Technology Sepuluh Nopember, Jl. Arief Rahman Hakim, Surabaya 60111, Indonesia
[b] Department of Physics, Faculty of Mathematics and Sciences, Semarang State University, Jl. Raya Sekaran Gunung Pati, Semarang 50221, Indonesia

ARTICLE INFO

ABSTRACT

This paper reports the synthesis and structural, microstructure, and dielectric characterizations of nanosized forsterite powders and their ceramics. Forsterite powder was synthesized by the mechanical activation of starting materials magnesium oxide (MgO) and amorphous silica (SiO_2) powders followed by calcination at 950 °C. The amorphous silica powder was obtained by processing local silica sand. The compound analysis of forsterite powder was performed by FTIR spectroscopy, phase analyses by XRD, and the particle size was found by TEM. The ceramics were synthesized by uniaxially pressing the powder and then sintering it at 950, 1050, 1150, and 1200 °C. Characterization of the ceramics included microstructure, diameter shrinkage, density, porosity, dielectric constant and quality factor. Results showed that the synthesized powder consisted of nanosized (ca. 55 nm) forsterite (Mg_2SiO_4) as the main phase, accompanied by protoenstatite ($MgSiO_3$), periclase (MgO), and low cristobalite (SiO_2) as minor phases. The sintered ceramics exhibited improved forsterite weight fraction with a maximum of 99.3% after sintering at 950 °C. Furthermore, with the increase in sintering temperature from 950 to 1200 °C, the density of the ceramics increased from 1.6 to 2.5 g cm^{-3} and also led to grain growth from 56 to 277 nm. Furthermore, their 10-GHz dielectric constants (ε'_r) were relatively low, i.e., between 6.0 and 13.3. In addition, all the ceramic samples had a loss factor tan δ < 0.0004 and a quality factor $Q \times f$ > 1000 GHz, which indicates that the dielectric properties of all the samples can be promoted as those of millimeter-wave candidate materials.

1. Introduction

Forsterite (Mg_2SiO_4) has been the topic of intense exploration because of its potential applications in the electronics, communications, and refractory industries, mainly due to its low electrical conductivity and high melting temperature [1,2]. Mg_2SiO_4 could also be used as millimeter-wave components in the future, because it offers a low dielectric constant of about 6.8 [3] and a relatively high $Q \times f$ value of up to 270,000 GHz [4,5]. Forsterite can be synthesized using various starting materials and methods. In general, commercial products were used as starting materials to produce forsterite powders [6–8], either in micro- or nanoscale. Furthermore, some researchers have also used low-grade or natural starting materials, such as rice husk ash [9,10], fumed silica [11], or silica sand [12,13] as the silica source. In most cases, the synthesis of forsterite powder required a relatively high temperature, ca. > 1000 °C. The synthesis of pure nanocrystalline forsterite powder was also possible. For example, by using magnesium nitrate and tetraethyl orthosilicate (TEOS) as the raw materials, as small as 30 nm forsterite nanoparticles were obtained by the sol–gel combustion

method [8] at a calcination temperature of 1100 °C. Another example is that by using magnesium carbonate and silicon dioxide as the raw materials, forsterite powder with an average particle size of 50–60 nm was synthesized [14,15]. Some researchers had introduced a mechanical activation by ball milling for 10–100 h prior to firing at 1200 °C or above [16,17]. They could successfully improve the mechanical properties and develop microstructures of forsterite powder. It is obvious that the keys for the synthesis of forsterite nanopowder are the type of raw materials, processing method, and activation energy prior to calcination. The protocol is consequently important to be followed; however, in this study, we concern on using natural silica sand as the source of silica and lower calcination temperature for such synthesis of nanocrystalline powder.

The above-mentioned applications of forsterite, in general, require forsterite in ceramic form. Previously, forsterite ceramics were produced from the raw materials or from forsterite powders, which were subject to pressing and followed by sintering [16–18]. Nevertheless, the sintering also required a temperature of more than 1200 °C [13]. Moreover, the ceramics exhibited forsterite with a microcrystalline size

---

[5,19,20]. The ceramics had a dielectric constant of 6.2–7.7 and a quality factor $Q \times f$ of 10,000–270,000 GHz [3,5,19,21,22]. These properties categorized them as a low dielectric constant and high quality factor materials. The synthesis of nano-forsterite ceramics, perhaps, has not been in the literature – so as too their physical and dielectric characters. It is therefore urgent to perform an investigation on fulfilling the disparity.

In this paper, we report our attempt to maintain the nanostructural characteristics of forsterite nanopowders to produce nano-forsterite ceramics by pressing the powder and then sintering it at a relatively low temperature, i.e., 950–1200 °C. The dielectric properties of the ceramics were characterized under a broad X-band frequency range (8–12 GHz). Variations in the phase composition, density, and microstructure of the ceramics [23–25] were also examined.

2. Experiment

Natural silica sand from Tanah Laut, South Kalimantan, was used as the silica source and was purified and processed to obtain an amorphous silica powder (denoted as ATL powder in this paper) as one of the starting materials, as reported previously [12,26]. The other starting material was MgO powder (Merck); it was heated at 400 °C for 30 min to remove residual water. The ATL and the treated MgO powders were mixed at a molar ratio of 1:2 for 3 h in ethanol. The slurry was then dried prior to calcination at 950 °C for 4 h in a Carbolite RHF-1400 furnace. The heating rate was controlled in five steps, i.e., 29, 23, 16, 9, and 6 °C s^{-1}, to optimize the formation of forsterite nanopowder (denoted as FTL powder). The calcination temperature was determined by the thermal analysis using the Mettler Toledo TGA/DSC1 Stare System. The formation of forsterite compound was confirmed by the spectral analysis of Perkin Elmer Frontier FTIR spectroscopy data through comparison of the calcined powder with the starting materials. KBr was used as a transparent background because it has a 100% transmittance around 4000–400 cm^{-1} range of wave. Therefore, it does not exhibit absorption in this range. Next, to produce nano-forsterite ceramics, the FTL powder was mixed with polyvinyl alcohol powder at 3% by weight as a binder and then uniaxially pressed at 4500 N prior to sintering. The compacted samples were sintered at 950, 1050, 1150, and 1200 °C for 4 h (denoted as FTLP950, FTLP1050, FTLP1150, and FTLP1200, respectively).

The phase compositions of the powders and ceramics were characterized by X-ray X′Pert Diffractometer (Philips). XRD measurements were made using a Cu-K$_\alpha$ radiation tube in a 2θ range from 15° to 90° and step size of 0.02°. Phase composition and crystallite size were estimated by the Rietveld-based Rietica [27] and Maud programs [28], respectively. A transmission electron microscope (FEI Tecnai-T20) was used to explore the microstructure of nano-forsterite powders. The TEM observation conditions were as follows: bright field image mode, 200 kV accelerating voltage, and 680 mm camera length for electron diffraction. Furthermore, the microstructure of the nano-forsterite ceramics was examined using a SEM (FEI Inspect-S50) at 20 kV. The bulk density and apparent porosity of the samples were obtained according to the Archimedes principle. The relative permittivity was measured by a vector network analyzer (VNA) using an open-ended rectangular waveguide probe system. The VNA was set for non-destructive testing to characterize the dielectric properties of the test samples. A transmission phase-shift method was used where an Advantest R3770 VNA (supporting frequencies from 300 kHz to 20 GHz) was connected to an A-INFOMW WG P/N 90WCAN rectangular waveguide. Two parameters of measurement were set up on both phase shift and S-parameter at 0.875 mm in thickness of the sample, which operated at the fundamental transverse electric $((TE)_{10})$ mode at 8.0–12.0 GHz. The relative complex permittivity of the samples was then calculated using a series of formulations as provided in the literature [29].
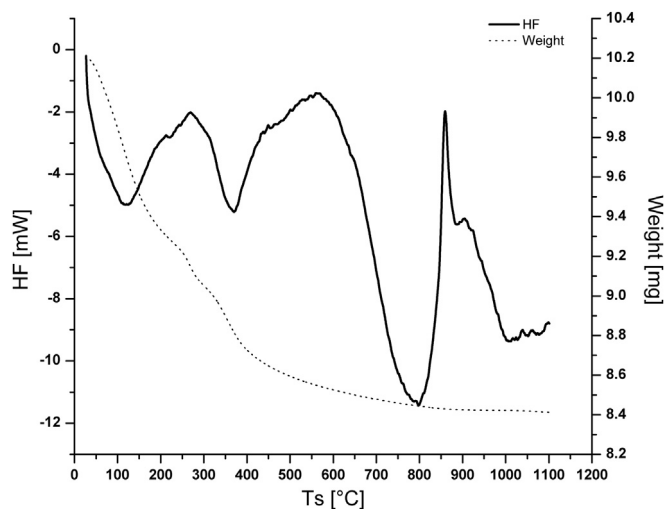

Fig. 1. Thermal behavior of the dried mixture from room temperature to 1100 °C.

3. Results and discussion

3.1. Structure and microstructure of forsterite powders

The differential scanning calorimetric and thermal gravity (DSC/TG) plots of the ball-milled mixture of amorphous silica and magnesium oxide are shown in Fig. 1. The TG traces exhibited a total weight loss of approximately 17% during heating. It decreased dramatically below 500 °C and relatively slowly until 900 °C. The weight loss curve revealed three main stages. First, a weight loss of approximately 11% at < 300 °C was observed because of the removal of free water. Second, a weight loss of approximately 4% observed at 300–600 °C was associated with the removal of water in $Mg(OH)_2$. Third, a weight loss of approximately 2% at 600–1100 °C was probably because of the loss of residual species in amorphous silica [30]. The DSC plot also shows three endothermic peaks, i.e., around 110, 370, and 780 °C. The first two peaks can be attributed to the above-mentioned water releases, while the last can be attributed to the crystallization of silica. Furthermore, there are two exothermic peaks at approximately (1) 860 °C, which may be associated with the formation of forsterite, and (2) 905 °C, which may be due to the formation of proto-enstatite [30]. The enthalpy of forsterite formation in our work was $\Delta H_{860C} = -48.39$ kJ/mole, which was calculated using heat flow [31] of the DSC curve. The required formation energy for forsterite in our case was clearly lower than that in the $MgCO_3$–SiO_2 system [30], which was 60 kJ/mole. We then chose 950 °C as the calcination temperature.

Fig. 2 shows the FTIR spectrum of the starting materials and the calcined powder. It is very clear that there are differences in the peaks of vibration between the samples. As shown in the figure, the FTIR absorption curves record some absorption bands of MgO, ATL, and FTL, which were measured at room temperature. Peak J at 638 cm^{-1} is associated with Mg-O binding, thereby confirming the presence of MgO [32]. Furthermore, the amorphous silica ATL sample showed four peaks at M = 1100 cm^{-1}, N = 963 cm^{-1}, O = 799 cm^{-1}, and P = 479 cm^{-1} which indicate the asymmetric stretching vibration of LO modes for Si-O-Si, symmetric stretching for Si-O-Si, asymmetric stretching for Si-O, and symmetric stretching for Si-O, respectively [33]. The forsterite FTL powder exhibits FTIR characteristics different from those of MgO and amorphous silica. As can be seen from Fig. 2, the FTL sample showed peaks at Q, R, S, T, U, and V, which match with those found by Kharaziha [34]. These peaks are related to the forsterite at Q = 1010 cm^{-1}, R = 896 cm^{-1}, S = 866 cm^{-1} (SiO$_4$ stretching), T = 618 cm^{-1} U = 523 cm^{-1} (SiO$_4$ bending), and V = 467 cm^{-1} for MgO$_6$ octahedral. In addition, the OH vibrational strain peak at C = 3448 cm^{-1} was visible in the FTL sample, thus indicating that it
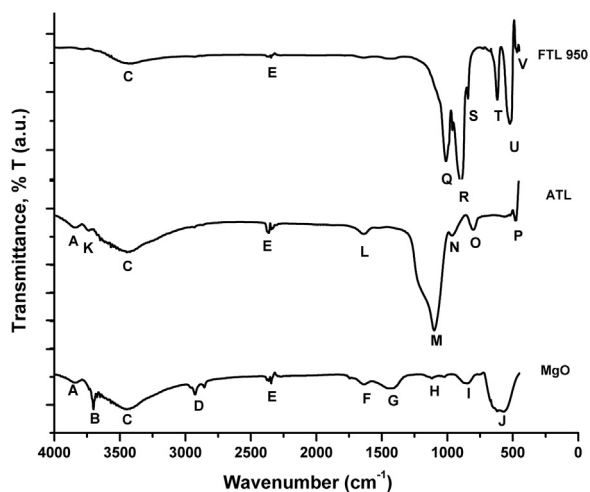
Fig. 2. FTIR patterns of the starting materials (MgO and ATL powders) and FTL powder at room temperature.

absorbs H_2O [35]. All the above analysis results suggest that a new compound has been formed in this sample after calcination. We expected the new compound to be forsterite, and the following XRD examination proves it.

Fig. 3 shows the XRD patterns of the FTL powder. The major identified phase was forsterite (Mg_2SiO_4, PDF# 34-0189), as expected. Thus, forsterite can be synthesized from amorphous silica and magnesia commercial powders at a calcination temperature of 950 °C. In addition, secondary phases, namely periclase (MgO, PDF# 45-0946), proto-enstatite ($MgSiO_3$, PDF# 74-816), and low-cristobalite (SiO_2, PDF# 82-1232) were present. Moreover, from the broadening of the XRD line shapes, the average crystallite size of the forsterite powder can be predicted [36]. The diffraction peak width of forsterite was relatively broad, ca > 0.2° 2θ, which indicates that the crystallite size of forsterite is nanometric. The TEM image of the associated powder (Fig. 4a) also revealed the presence of numerous grains, which indicates that the FTL sample contains nanopowders. The TEM average crystallite size was 55(6) nm. The electron-diffraction pattern (Fig. 4b) confirmed the formation of forsterite crystals in the powder.

A quantitative analysis of the powder showed that forsterite was dominant, i.e., of 81.0(10) wt%, while the secondary phases periclase, low-cristobalite, and proto-enstatite were found to be of 10.9(2), 3.2(7), and 4.9(6), respectively. It is worth noting that the addition of 3 wt% PVA had enhanced the formation of forsterite. The secondary phases were often encountered in the synthesis of forsterite powders as
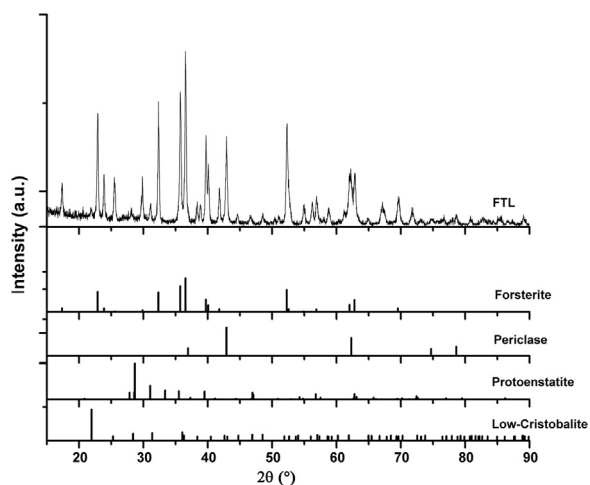
reported before [17,30]. The largest difference between our and these studies is that we used 3 h of milling time and 950 °C as the calcination temperature, while they used more than 10 h of milling and above 1000 °C as the calcination temperature. Furthermore, the lattice parameter values of forsterite in our powder were $a = 4.750$ Å, $b = 10.189$ Å, and $c = 5.978$ Å, which are in good agreement with the literature values [37]. Thus, our synthesis method can be claimed as a relatively efficient process in the fabrication of a nanometric forsterite powder (Table 1).

3.2. Characterization of forsterite ceramics

The XRD patterns of the sintered ceramics (FTLP950-1200) are given in Fig. 5. All the patterns show that the samples consisted of forsterite and periclase as major and minor phases, respectively. Here, both low cristobalite and protoenstatite were not detected anymore. Rietveld analysis revealed that the ceramics contained more than 90 wt % forsterite, see Table 2. This implies that the ceramics have a higher forsterite content than the powder. Thus, the sintering process stimulates the rearrangement of secondary phases in the forsterite powder to form forsterite according to the following reactions:

$$a - SiO_2(s) \quad + \quad 2MgO(s) \rightarrow \ Mg_2SiO_4(s) \tag{1}$$

$$MgSiO_3(s) + MgO(s) \ \rightarrow \ Mg_2SiO_4(s) \tag{2}$$
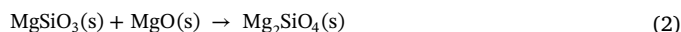
where a-SiO_2 is amorphous silica.

There are several X-ray diffraction peak characters that change with temperature, as shown in Fig. 5. First, the periclase peak intensity at 2θ ≈ 43° increased with increase in sintering temperature, while the forsterite peak intensity decreased. Table 2 presents the forsterite content, which can be as high as 99.3 wt%, in the FTLP950 sample, and the rest is periclase. The forsterite content decreased up to 91.7 wt% for the sample at 1200 °C. Because only two crystalline phases were present, this result indicates that the phase composition of periclase increased, which is provided in Table 2.

Second, a diffraction "hump" between 40° and 50° 2θ (indicated by a large arrow) became more obvious, which implies that more amorphous phase appears after sintering at higher temperature. We assume here that some forsterite have decomposed into its components, i.e. silica and periclase. However, this phenomenon has not been observed by others. To make sure that the decomposition has occurred, we performed an elemental analysis using an energy-dispersive spectrometer to find the Mg/Si content ratio of all the samples. The tests were done at six different points. The results are shown in Table 2, and Mg/Si weight ratio was the same, ca. 1.7, for all the samples at all testing points. The ratio was as expected because the molecular weight of Mg is 24 and that of Si is 28. Because forsterite has two magnesium and one silicon, the ratio is 48/28 or 1.71. The above observation and analysis lead to a conclusion that forsterite can decompose as follows:

$$Mg_2SiO_4(s) \rightarrow \ SiO_2(a) + 2MgO(s) \tag{3}$$

where SiO_2 (a) is amorphous silica. The XRD data of the amorphous content were further analyzed as follows:

- A sample of presumably 100% crystalline of rutile powder would give standard background intensity (I_{bs}) – this should be a laboratory-dependent result.
- Sample FTLP950 is assumed the reference sample because it exhibits the lowest XRD background. Its measured background intensity (I_{950}) is a summation of I_{bs} and I_{br}.
- Other samples exhibit a background intensity of I_B, which is given by $I_{br} + I_a$, where I_a is the amorphous background of the samples. The amorphous content of the sample is then $\frac{I_B - I_{br}}{I_{br}}$.

This approach showed an increase in amorphous content with increase in sintering temperature from 2.5 to 12.0 wt% – see Table 2.
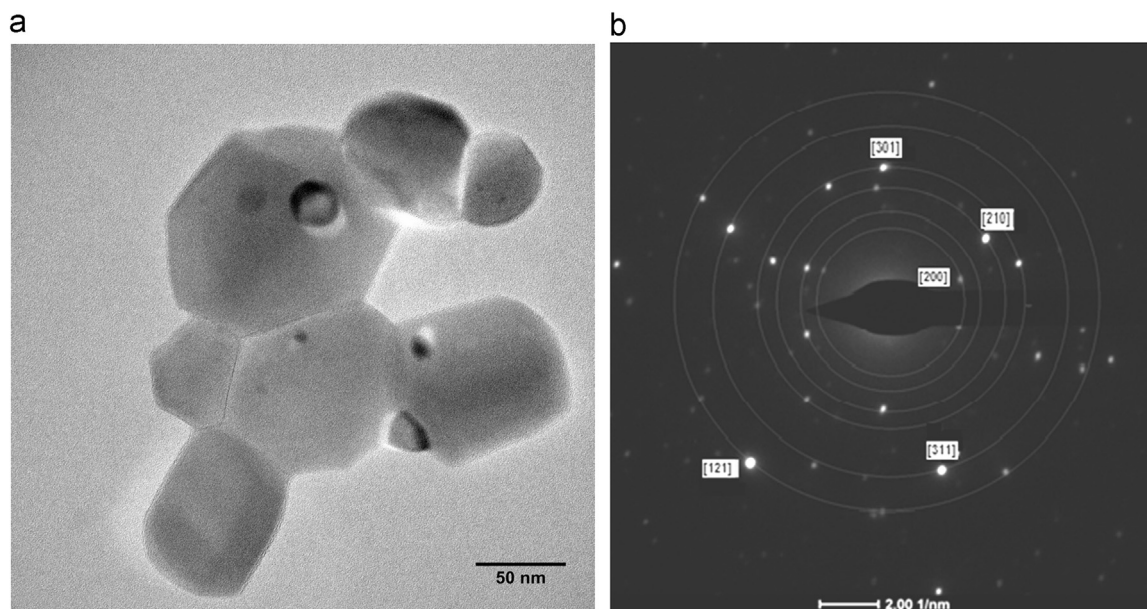

Fig. 3. XRD pattern (CuK$_\alpha$ radiation) of the FTL powders.

Fig. 4. a) Bright field TEM image and b) the electron diffraction pattern of FTL powder.

Table 1
Positions of the all functional groups present in the forsterite powder compared to those found in the literature.

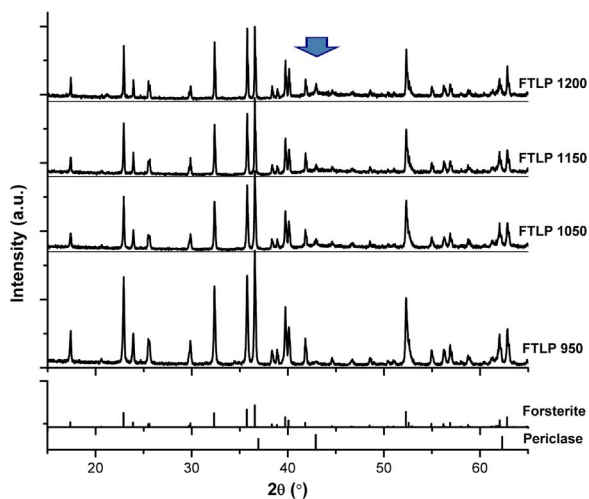| Functional structure	Wavenumber (cm^{-1})		
	Peak Mg$_2$SiO$_4$	Kharaziha [34]	Kamalian [33]
MgO$_6$	467	475	483
SiO$_4$ Stretching	866, 896, 1011	830–1000	910–1029
SiO$_4$ Bending	523, 618	500–620	488–643

Fig. 5. XRD pattern (CuK$_\alpha$ radiation) of ceramic forsterite at different sintering temperatures, each sintering was performed for 4 h. Arrow indicates "hump" zones, which can be related to the presence of amorphous silica due to forsterite decomposition.

The third characteristic is associated with the peak broadening of forsterite, which tends to decrease with increase in temperature. By using the MAUD software, which is also based on Rietveld method, with an appropriate instrument correction, we found an increase in the crystallite size of forsterite (Table 2). The values remained nanometric for the 950 and 1050 samples, i.e., 56 and 105 nm, respectively, but became sub-nanometric, i.e. 240 and 277 nm, for the others. Thus, we have successfully synthesized nano-forsterite ceramics.

We further scrutinized the X-ray diffraction peak characteristics in terms of the lattice parameters of forsterite. Table 2 shows that each lattice parameter value increased with the increase in sintering temperature. It is known from the literature that forsterite has an orthorhombic structure with a space group of *Pbnm* and lattice parameter values of $a = 4.756$ Å, $b = 10.207$ Å, and $c = 5.990$ Å [37]. By using a simple calculation of the volume of an orthorhombic crystal, it was found that the forsterite room-temperature crystal volume increased by 0.07%, 0.13%, and 0.18% with the increase in sintering temperature. In ceramic systems, room-temperature cell expansions are in general found in doped materials, e.g. [38]. In our case, where dopant was absent, the increase in the room-temperature cell volume may be because of the appearance of the amorphous silica. The raw powder contained 81.0 wt% forsterite. Sintering at 950 °C resulted in 99.3 wt% forsterite and only 0.7 wt% periclase – refer to Table 2 for phase compositions. This porous ceramic exhibited forsterite with a cell volume of 289.5 Å^3. As the sintering temperature increased, forsterite decomposed into amorphous silica and periclase (crystals). Higher sintering temperature caused higher amorphous silica content. The amorphous silica is a glassy phase, which may favor the expansion of the neighboring crystallite cells. The crystallite cells remained expanding although the sintering temperature had been brought down to room temperature. Therefore, because a large amount of amorphous silica was found at higher sintering temperature, the room-temperature cell volume of (crystallite) forsterite increased.

The SEM images of the polished surface of the FTLP950-1200 samples are presented in Fig. 6. It can be seen from Fig. 6a that FTLP950 sample, which contains 99.3 wt% forsterite, displays particles with a sheet-like structure of approximately 50 nm in thickness. This size is in accordance with the XRD and TEM results. The porosity of this sample was relatively high, i.e., approximately 41% (see Fig. 7). After sintering at 1050 °C, the sheet-like structures transformed into larger orthorhombic forsterite particles (Fig. 6b) with less sheet-like structures. At a sintering temperature of 1150 °C, the sheet-like structures disappeared, and this was followed by the formation of even larger orthorhombic forsterite particles with a smaller degree of porosity (approximately 17%). Fig. 6d shows the micrograph of the sample sintered at 1200 °C. The orthorhombic particles became more dominant and the porosity reduced to 14%.

The bulk density and apparent porosity of the FTLP sintered ceramics are shown in Fig. 7. An increase in bulk density and shrinkage and

Table 2

Phase composition, lattice parameters and crystallite size of forsterite ceramics at various sintering temperatures. Figures in parentheses are the estimated standard deviations of the values to the left.

| Sample	Amorphous wt%	Mg/Si	Periclase wt%	Forsterite				
				wt%	a	b	c	D(nm)
FTLP950	0	1.7(1)	0.7(1)	99.3(1)	4.7506	10.1939	5.9792	56(1)
FTLP1050	2.5	1.7(1)	4.9(2)	95.1(1)	4.7513	10.1967	5.9807	105 (1)
FTLP1150	9.1	1.7(1)	6.9(1)	93.1(1)	4.7516	10.1990	5.9829	240 (1)
FTLP1200	12.0	1.7(1)	8.3(1)	91.7(1)	4.7522	10.2007	5.9837	277 (8)

a decrease in apparent porosity with increase in temperature can be obviously seen from the figure. The changes in the physical properties of the ceramics can be attributed to the presence of forsterite, residual MgO particles, and the amorphous silica. A great increase in ceramic density was observed from 1.5 to 2.5 g cm^{-3}, while the apparent porosity decreased from 41.4% to 13.6%. Also, the shrinkage of the ceramics increased linearly with sintering temperature, i.e. 5–15% at the same range. The theoretical density of forsterite, periclase, and amorphous silica are 3.3, 3.6, and 2.2 g cm^{-3}, respectively [39]. Therefore, only approximately 85% theoretical density was achieved in this research. A study on the improvement of the densification of the ceramics at low sintering temperature is now underway.

3.3. Dielectric property

Fig. 8 shows the dielectric properties of the FTLP ceramics. The dielectric properties were measured using the VNA because the composite ceramics are porous. Fig. 8 shows that the higher sintering temperature, the higher the value. The ε_r' FTLP1200 ceramic was 13.3, which is more than twice that of FTLP950 sample. This finding can be explained as follows. In our case, the change in the ε_r' value of ceramics can be caused by four phenomena. First, the ε_r' change could be due to the change in phase composition. The ε_r' values of forsterite, periclase, and silica were 6.2, 9.6 and 4.,2 respectively [40]. Total ε_r' were calculated using the "rules of mixture" approach as follows:

$$\varepsilon_r' = \sum_i v_i \varepsilon_{ri}'$$

(4)

where v is the volume fraction and the subscripts i represent main phase
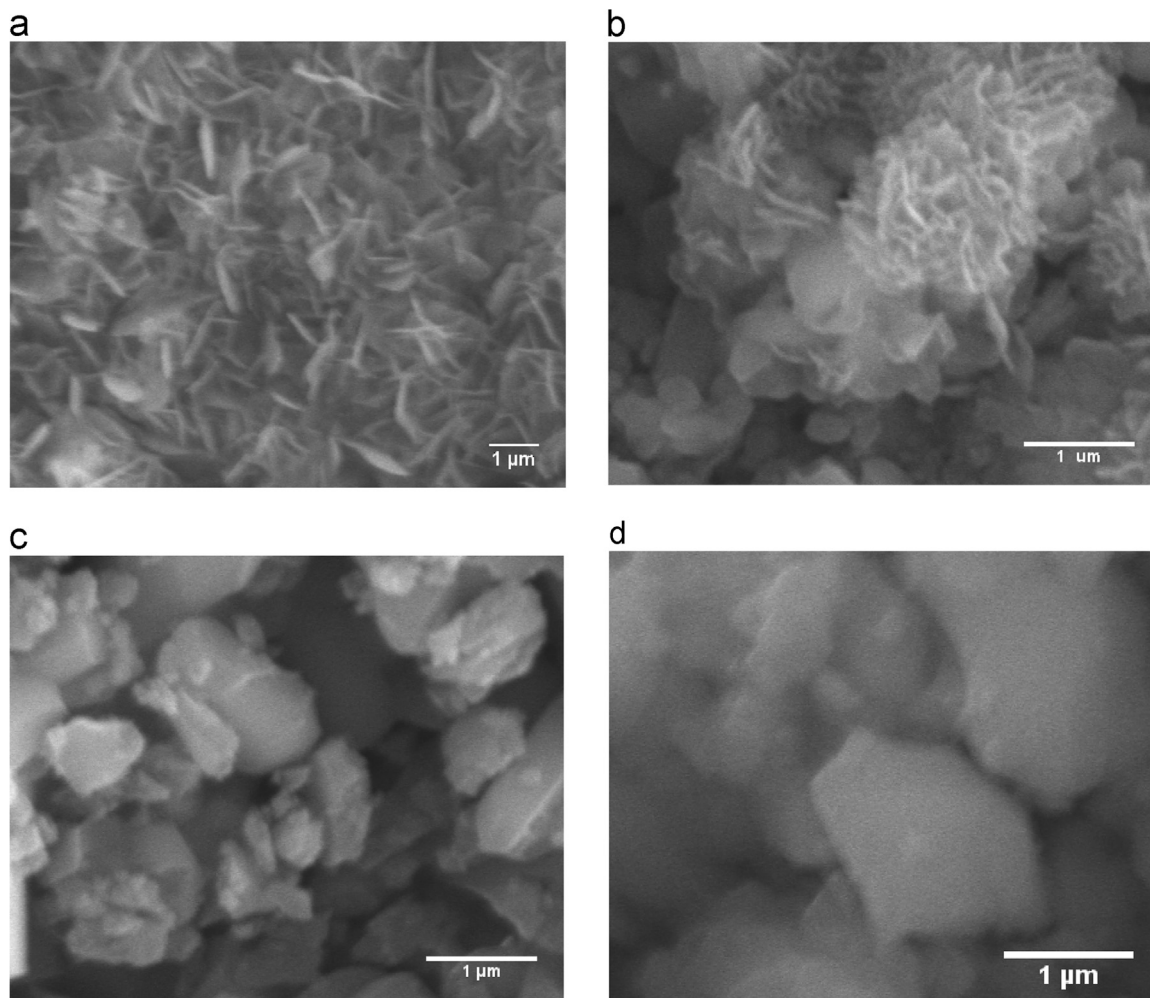
Fig. 6. SEM image of forsterite ceramics a) FTLP 950, b) FTLP 1050, c) FTLP 1150, and d) FTLP 1200, Holding time = 4 h holding time.
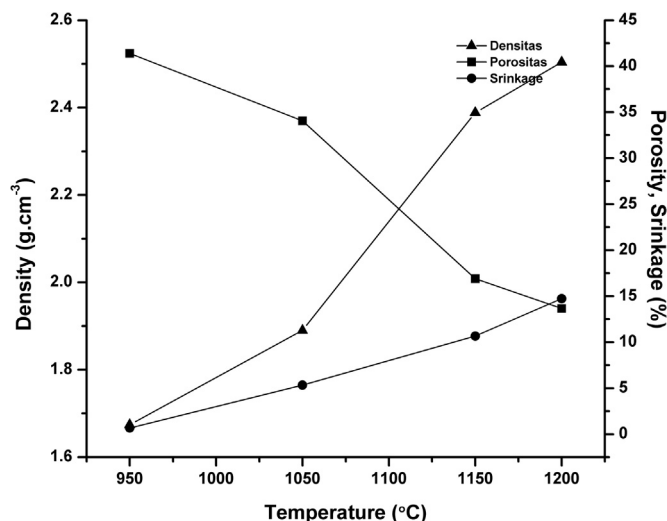
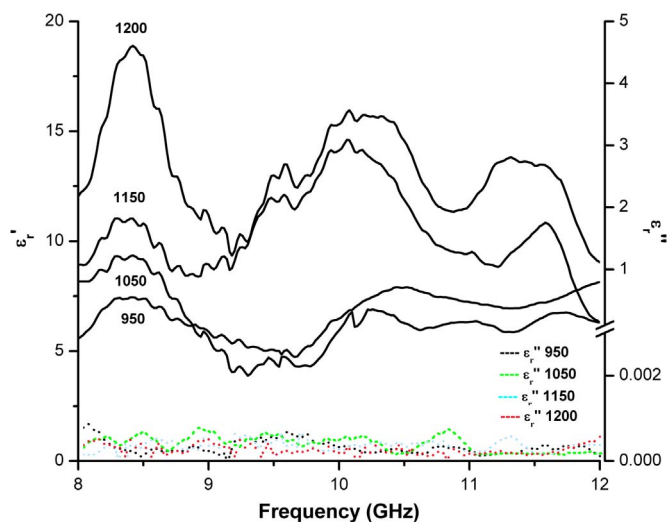**Fig. 7.** Apparent density and apparent porosity of forsterite ceramics.

Fig. 8. A relative permittivity ε_r' and attenuation loss tangent ε_r'' of forsterite in the X-band region after the calculation of all the available data from VNA measurement using the NRW algorithm by setting the permeability as 1 ($\mu = 1$).

Table 3
Calculated real dielectric constant (Eq. (4)), experimental real dielectric constants (averaged and at 10 GHz), experimental imaginary dielectric constant (at 10 GHz) and quality factor (at 10 GHz).

Sample	Calculated ε_r'	Experiment			
		ε_r'(average)	ε_r'(10 GHz)	ε_r'' (10 GHz)	$Q \times f$ (10 GHz)
FTLP950	6.2	6.0	7.5	0.0019	40,193
FTLP1050	6.3	7.1	8.6	0.0022	39,808
FTLP1150	6.2	10.5	14.5	0.0048	29,715
FTLP1200	6.1	13.3	17.9	0.0041	43,759

and secondary phases. The ε_r' values of FTLP950, FTLP1050, FTLP1150, and FTLP1200 samples were 6.2, 6.3, 6.2, and 6.1, respectively. These values are much lower than the measured results, implying that phase composition is not the only contributor for the varying ε_r' values. We observed the second reason for change in ε_r' value may be because of the density of the ceramics. Denser ceramics (which is inverse of porosity, as seen in Fig. 7) exhibited higher ε_r' value [13,41]. They found that for SiN ceramics, an increase in density as much as 33% (from 2.4 to

3.2 g cm^{-3}) was followed by an increase in the ε_r' up to 50% (from 5.7 to 8). In our case, for example, for FTLP 950 and 1200 samples, the density increased from 1.9 to 2.5 (approximately 31%), and the ε_r' value increased from 6 to 13.3 or more than 200%. Comparing this increase with that in the SiN ceramic, we found another reason for the ε_r' increase. Third, amorphous silica content tends to reduce the dielectric constant. The FTLP1200 ceramic contained 12 wt% (equals to 14 vol%) amorphous silica higher than the FTLP950. Because the ε_r' value of silica is 4.3 [42,43], the ε_r' of the FTLP1200 sample reduced but only by approximately 3%, i.e., from 6.2 to 6.0 (see Table 3). We argue here that the fourth contributor, i.e., the most important phenomenon, responsible for the ε_r' increase is the forsterite crystal size. The effect of crystallite size (or grain size) on the ε_r' had been studied by several researchers [24,25,43]. For $Zn_{0.7}Mg_{0.3}TiO_3$, when the grain size increased by approximately 13%, the ε_r' increase was 4.5%. In our samples, forsterite as the major phase exhibited an increase in crystallite size from 56 nm for the FTLP950 to 277 nm for the FTLP1200. The dimension expansion was huge, which resulted in a very high increase in ε_r'. Therefore, synthesizing nano-forsterite ceramics creates lower ε_r' value materials.

Frequency dependence of dielectric constant, as shown in Fig. 8, is another important result to report. For FTLP950 and FTLP1050 samples, the dielectric constants were relatively independent of frequency, with average values of approximately 6 and 7.1 respectively, see Table 3, while for FTLP1150 and FTLP1200 samples, the ε_r' values significantly fluctuated. This result suggests that a careful attention should be paid while implementing the material for applications. At this stage, a great example is only applicable to the ideal case. Normally, the dielectric constant ε_r' can be accurately predicted at the center operating frequency. So, the dielectric constant was predicted at the center operating frequency of a wave-guide [29], where for X-band, the frequency $f_{center} = 10$ GHz, and the quality factor $Q \times f$ for this frequency can be calculated. To acquire the quality factor, the loss factor should be examined.

For all samples, the energy dissipation occurs when microwave energy was absorbed by the material. As shown in Fig. 8, the colored curves were tan δ or $\varepsilon_r''/\varepsilon_r'$ which valued < 0.0004. These results indicate that all the FTLP950-1200 samples had a very low loss at the X-band frequency [43].

The ε_r'' values at 10 GHz of the FTLP950-1200 ceramics are presented in Table 3. It generally increased with the increase in sintering temperature. The literature points out dependence of ε_r'' value on lattice vibration, density, grain boundaries, and secondary phases [44], but their individual contribution could not be determined precisely. In our case, the decrease in ε_r'' value is believed to be because of all these effects. However, we also could not determine exactly their individual roles.

Table 3 shows that the $Q \times f$ values range between approximately 29,000 and 44,000. As shown in the table, the highest quality factor was approximately 44,000 GHz for the FTLP1200 sample. The FTLP950 sample exhibits relatively high $Q \times f$ value which is similar to the FTLP1200 but higher than those of other two ceramics. The main contributor for the high $Q \times f$ value for FTLP950 sample is presumably the nanometric crystal size of forsterite as also found for the ε_r' value. This consequence can be associated with the pair ε_r' and ε_r'' values for each ceramic because $Q \times f = \frac{\varepsilon_r'}{\varepsilon_r''}$. This value was comparable to those for other pure forsterite ceramics, which were between 40,000 and 240,000 GHz [19,45,46]. These results indicate that the ceramics are appropriate for millimeter-wave and substrate applications.

4. Conclusion

Nano-forsterite ceramics were successfully fabricated using purified amorphous silica from natural silica sand as the source of silica and magnesium oxide. The increase in sintering temperature caused a

decrease in the weight fraction of forsterite by up to 15% of the nearly 100% nano-forsterite 950 °C ceramic. The increase in sintering temperature was followed by the decomposition of forsterite into periclase and amorphous silica, an increase in the density of the ceramics from approximately 50% to 85% theoretical density, and an increase in XRD crystallite and SEM grain sizes. The average ε_r' value increased by more than 200% than that at the lowest sintering temperature but still showed a low dielectric character. Because the synthesized ceramics have a low relatively dielectric constant ($\varepsilon_r' < 20$) and a low dielectric loss ($\varepsilon_r''/\varepsilon_r' < 0.0004$), they are good candidates for low-loss microwave applications.

Acknowledgement

References

[1] H. Ohsato, T. Tsunooka, T. Sugiyama, K. Kakimoto, H. Ogawa, Forsterite ceramics for millimeterwave dielectrics, J. Electroceram. 17 (2006) 445–450.

[2] W.R. Bratschun, A.J. Mountvala, A.G. Pincus, Uses of Ceramics in Microelectronics a Survey, US Government Printing Office, Washington, D.C., 1971.

[3] S.T. Lee, Y.H. Jo, H. Kim, D.H. Youn, I.J. Choi, S.H. Key, C.Y. Kang, W.S. Hong, Y.S. Cho, Grain boundary segregation and microwave dielectric properties of low loss $Mg_{1.5}Zn_{0.5}SiO_4$ ceramics containing Bi_2O_3, Adv. Appl. Ceram. 109 (2010) 367–372.

[4] K.X. Song, X.M. Chen, X.C. Fan, Effects of Mg/Si ratio on microwave dielectric characteristics of forsterite ceramics, J. Am. Ceram. Soc. 90 (2007) 1808–1811.

[5] K.X. Song, X.M. Chen, C.W. Zheng, Microwave dielectric characteristics of ceramics in Mg_2SiO_4–Zn_2SiO_4 system, Ceram. Int. 34 (2008) 917–920.

[6] H.B. Bafrooei, T. Ebadzadeh, H. Majidian, Microwave synthesis and sintering of forsterite nanopowder produced by high energy ball milling, Ceram. Int. 40 (2014) 2869–2876.

[7] S.M. Mirhadi, A. Forghani, F. Tavangarian, A modified method to synthesize single-phase forsterite nanoparticles at low temperature, Ceram. Int. 42 (2016) 7974–7979.

[8] R. Choudhary, M. Prasanth, J. Vecstaudza, M.J.Y. Gascón, H.P. Sánchez, N. Ramesh, J. Locs, S. Swamiappan, Preparation of nanocrystalline forsterite by combustion of different fuels and their comparative in-vitro bioactivity, dissolution behaviour and antibacterial studies, Mater. Sci. Eng. C 77 (2017) 811–822.

[9] M.I. Martin, F. Andreola, L. Barbieri, F. Bondioli, I. Lancellotti, J.M. Rincón, M. Romero, Crystallisation and microstructure of nepheline–forsterite glass ceramics, Ceram. Int. 39 (2013) 2955–2966.

[10] S.K.S. Hossain, L. Mathur, P. Singh, M.R. Majhi, Preparation of forsterite refractory using highly abundant amorphous rice husk silica for thermal insulation, J. Asian Ceram. Soc. 5 (2017) 82–87.

[11] L. Chen, G. Ye, Q. Wang, B. Blanpain, A. Malfliet, M. Guo, Low temperature synthesis of forsterite from hydromagnesite and fumed silica mixture, Ceram. Int. 41 (2015) 2234–2239.

[12] U. Nurbaiti, Triwikantoro, M. Zainuri, S. Pratapa, Synthesis of microforsterite using derived-amorphous-silica of silica sands, AIP Conf. Proc. 1725, 2016, p. 020056.

[13] S. Pratapa, W.D. Handoko, U. Nurbaiti, Mashuri, Synthesis and characterization of high-density B_2O_3-added forsterite ceramics, Ceram. Int. 43 (2017) 7172–7176.

[14] M.H. Fathi, M. Kharaziha, Mechanically activated crystallization of phase pure nanocrystalline forsterite powders, Mater. Lett. 62 (2008) 4306–4309.

[15] S.N. Hosseini, H.S. Jazi, M. Fathi, Novel electrophoretic deposited nanostructured forsterite coating on 316L stainless steel implants for biocompatibility improvement, Mater. Lett. 143 (2015) 16–19.

[16] K.Y.S. Lee, K.M.C. Chin, S. Ramesh, J. Purbolaksono, M.A. Hassan, M. Hamdi, W.D. Teng, Characterization of forsterite ceramics, Ceram. Process. Res. 14 (2013) 131–133.

[17] S. Ramesh, A. Yaghoubi, K.Y.S. Lee, K.M.C. Chin, J. Purbolaksono, M. Hamdi, M.A. Hassan, Nanocrystalline forsterite for biomedical applications: synthesis, microstructure and mechanical properties, J. Mech. Behav. Biomed. Mater. 25 (2013) 63–69.

[18] A.B. Rani, A.R. Annamalai, M.R. Majhi, A.H. Kumar, Synthesis and characterization of forsterite refractory by doping with kaolin, Int. J. ChemTech Res. CODEN 6 (2014) 1390–1397.

[19] T. Tsunookaa, M. Androua, Y. Higashida, H. Sugiura, H. Ohsato, Effects of TiO_2 on sinterability and dielectric properties of high-Q forsterite ceramics, J. Eur. Ceram. Soc. 23 (2003) 2573–2578.

[20] M. Ando, Y. Higashida, N. Shibata, Forsterite-based ceramics for microwave application with low loss and low temperature coefficient of relative permittivity, J. Jpn. Soc. Powder Powder Metall. 48 (2001) 784–789.

[21] Z. Fu, J. Ma, P. Liu, Y. Li, X. Zhang, Crystal structure and microwave dielectric properties of middle-temperature-sintered $Mg_2Si_{(1-x)}V_xO_4$ ceramics, J. Electroceram. 36 (2016) 82–86.

[22] L. Li, Y. Wang, W. Xia, X. He, P. Zhang, Effects of Zn/Mg ratio on the microstructure and microwave dielectric properties of $(Zn_{1-x}Mg_x)_2SiO_4$ ceramics, J. Electron. Mater. 41 (2012) 684–688.

[23] C. Zhang, R. Zuo, J. Zhang, Structure-dependent microwave dielectric properties and middle-temperature sintering of forsterite $(Mg_{1-x}Ni_x)_2SiO_4$ Ceramics, J. Am. Ceram. Soc. 98 (2015) 702–710.

[24] G. Zang, J. Wang, C. Wang, Grain boundary effect on the dielectric properties of $CaCu_3Ti_4O_{12}$ ceramics, J. Phys. Appl. Phys. 38 (2005) 1824–1827.

[25] S.R. Kiran, G. Sreenivasulu, V.R.K. Murthy, V. Subramanian, B. Murthy, Effect of grain size on the microwave dielectric characteristics of high-energy ball-milled zinc magnesium titanate ceramics, J. Am. Ceram. Soc. 95 (2012) 1973–1979.

[26] U. Nurbaiti, F.A. Su'ud, D. Darminto, Triwikantoro, M. Zainuri, S. Pratapa, Synthesis of nano-forsterite powder by making use of natural silica sand, AIP Conf. Proc., 1710, 2016, p. 030037.

[27] B. Hunter, Rietica – a visual Rietveld program, Int. Union Crystallogr. Comm. Powder Diffr. Newsl. 31 (2000) 20.

[28] L. Lutterotti, Total pattern fitting for the combined size-strain-stress-texture determination in thin film diffraction, Nucl. Instrum. Methods Phys. Res. B 268 (2010) 334–340.

[29] K.Y. You, L. Zahid, M.F.A. Malek, K.Y. Lee, E.M. Cheng, N.H.H. Khamis, Dielectric measurements for low-loss materials using transmission phase-shift method, J. Teknol. Sci. Eng. 77 (2015) 69–77.

[30] A. Douy, Aqueous syntheses of forsterite (Mg_2SiO_4) and enstatite ($MgSiO_3$), J. Sol-Gel Sci. Technol. 24 (2002) 221–228.

[31] C. Rathgeber, L. Miró, L.F. Cabeza, S. Hiebler, Measurement of enthalpy curves of phase change materials via DSC and T-History: when are both methods needed to estimate the behaviour of the bulk material in applications? Thermochim. Acta 596 (2014) 79–88.

[32] A.M. Hofmeister, E. Keppel, A.K. Speck, Absorption and reflection infrared spectra of MgO and other diatomic compounds, Mon. R. Astron. 345 (2003) 16–38.

[33] R. Kamalian, A. Yazdanpanah, F. Moztarzadeh, R. Ravarian, Z. Moztarzadeh, M. Tahmasbi, M. Mozafari, Synthesis and characterization of bioactive glass/forsterite nanocomposites for bone and dental implants, Ceram. – Silik. 56 (2012) 331–340.

[34] M. Kharaziha, M.H. Fathi, Synthesis and characterization of bioactive forsterite nanopowder, Ceram. Int. 35 (2009) 2449–2454.

[35] A. Hushur, M.H. Manghnani, J.R. Smyth, F. Nestola, D.J. Frost, Crystal chemistry of hydrous forsterite and its vibrational properties up to 41 GPa, Am. Mineral. 94 (2009) 751–760.

[36] S. Pratapa, L. Susanti, Y.A. Insany, Z. Alfiati, B. Hartono, Mashur, A. Taufiq, A. Fuad, Triwikantoro, S. Purwaningsih, E. Yahya, Darminto, XRD line-broadening characteristics of M-oxides (M = Mg, Mg-Al, Y, Fe) nanoparticles produced by coprecipitation method, AIP Conf. Proc., 1284, 2010, pp. 125–128.

[37] J.R. Smyth, T.C. McCormick, Crystallographic data for minerals, Miner. Phys. Crystallogr. Handb. Phys. Constants 2 (1995) 1–17.

[38] T.S. Velayutham, N.I.F. Salim, W.C. Gan, W.H.A. Majid, Effect of cerium addition on the microstructure, electrical and relaxor behavior of $Sr_{0.5}Ba_{0.5}Nb_2O_6$ ceramics, J. Alloy. Compd. 666 (2016) 334–340.

[39] T.J. Ahrens, Mineral Physics & Crystallography: A Handbook of Physical Constants, American Geophysical Union, Washington DC, 1995.

[40] W.D. Kingery, H.K. Bowen, D.R. Uhlmann, Introduction to Ceramics, John Wiley and Sons, New York, 1975.

[41] V.R.K. Murthy, S. Sundaram, B. Viswanathan (Eds.), Microwave Materials, Springer Berlin Heidelberg, Berlin, Heidelberg, 1994.

[42] R. Umemura, H. Ogawa, H. Ohsato, A. Kan, A. Yokoi, Microwave dielectric properties of low-temperature sintered $Mg_3(VO_4)_2$ ceramic, J. Eur. Ceram. Soc. 25 (2005) 2865–2870.

[43] S.J. Penn, N.M. Alford, A. Templeton, X. Wang, M. Xu, M. Reece, K. Schrapel, Effect of porosity and grain size on the microwave dielectric properties of sintered alumina, J. Am. Ceram. Soc. 80 (1997) 1885–1888.

[44] Y. Lv, R. Zuo, Y. Cheng, C. Zhang, Low-temperature sinterable (1-x) $Ba_3(VO_4)_2$–$xLiMg_{0.9}Zn_{0.1}PO_4$ microwave dielectric ceramics, J. Am. Ceram. Soc. 96 (2013) 3862–3867.

[45] K.X. Song, J.M. Xu, X.P. Hu, L. Zheng, Z.H. Ying, H.B. Qiu, Microwave dielectric properties of Al-substituted forsterite ceramics, in: Proceedings of the International Conference on Electrical and Control Engineering, 6, 2010, pp. 5862–5864.

[46] K.X. Song, X.M. Chen, Phase evolution and microwave dielectric characteristics of Ti-substituted Mg_2SiO_4 forsterite ceramics, Mater. Lett. 62 (2008) 520–522.